The Meteoritical Society

Meteoritics & Planetary Science 61, Nr 2, 272–284 (2026)
doi: 10.1111/maps.70094

New evidence on the formation conditions of the Libyan Desert Glass (Western Egypt): Clues from a dendritic zircon inclusion

Niccolò MAGNANI[1,2]*, Enrico MUGNAIOLI[2,3], Sofia LORENZON[2], Lidia PITTARELLO[4], Tatiana E. GORELIK[5], Matteo MASOTTA[2,3], and Luigi FOLCO[2,3]

[1]Dipartimento di Scienze dell'Ambiente e della Terra, Università di Milano-Bicocca, Milan, Italy
[2]Dipartimento di Scienze della Terra, Università di Pisa, Pisa, Italy
[3]Centre for Instrument Sharing of the University of Pisa, Pisa, Italy
[4]Mineralogisch-Petrographische Abteilung, Naturhistorisches Museum, Vienna, Austria
[5]Ernst Ruska-Centre for Microscopy and Spectroscopy with Electrons, Forschungszentrum Juelich, Juelich, Germany

***Correspondence**
Niccolò Magnani, Dipartimento di Scienze dell'Ambiente e della Terra, Università di Milano-Bicocca, Piazza della Scienza 4, Milan 20126, Italy.
Email: n.magnani5@campus.unimib.it

(Received 31 October 2025; revision accepted 06 January 2026)

Abstract–Libyan Desert Glass (LDG) is an ~29 million years old, silica-rich glass found in Western Egypt. Whether this glass formed in an impact cratering context associated with the hypervelocity collision of a cometary/asteroidal body or radiative heating during an airburst is debated. Determination of the formation temperatures and pressures of rare mineral components in LDG can provide key petrogenetic constraints on its origin. Here, we report the occurrence of a zircon inclusion, whose textural, chemical, and crystallographic features point to a rapid formation during solidification of the silica-rich LDG melt. The study was conducted combining dual beam microscopy, transmission electron microscopy, energy-dispersive X-ray spectroscopy, and three-dimensional electron diffraction. The inclusion is a few tens of micrometer in size and consists of dendritic branches of zircon arranged in a reticulate-cruciform texture. The high-silica glass filling interstices between dendrites have longer chemical bonds compared to matrix glass, as indicated by electron pair distribution function analysis, and is enriched in Al_2O_3. The lack of incongruent melt products (ZrO_2, SiO_2) suggests that the inclusion formed during cooling from supraliquidus conditions, by dynamic crystallization from an (immiscible) undercooled liquid droplet. Such droplet would derive from shock-induced melting of a precursor zircon grain, possibly mixed with the SiO_2-rich liquid formed by melting of the LDG precursor material. The formation model proposed for this inclusion does not allow us to discriminate between the two genetic processes proposed for LDG, but sets a new minimum to the liquidus temperature of the corresponding chemical system of ~2250°C.

INTRODUCTION

Libyan Desert Glass (LDG) is a natural glassy material first described more than 90 years ago in the Eastern Great Sand Sea, Western Egypt (Clayton & Spencer, 1933; Spencer, 1939; Weeks et al., 1984). Specimens are typically found within north–south trending, almost linear, interdune corridors, over the outcropping basement, represented by the Nubian Formation, mainly consisting of alluvial-plain sandstone units (Klitzsch, 1978). The size of LDG specimens ranges from millimeters to few tens of centimeters (e.g., Weeks et al., 1984). The color varies from bright yellow to yellow-greenish, pale yellow, whitish, or even pinkish

(Fröhlich et al., 2013). It is usually translucent although cloudy specimens are found as well. This cloudy appearance is attributed to the high abundance of vesicles and/or cristobalite inclusions (e.g., Fröhlich et al., 2013; Spencer, 1939). Another recurrent feature in some specimens is the compositional layering, that is, alternating bands of dark and pale glass. An age of about 29 *Ma* was determined for LDG via fission-track method (Bigazzi & De Michele, 1996; Storzer & Wagner, 1977).

Geochemically, LDG is a high-silica glass (~98 wt% SiO_2 average, Barnes & Underwood, 1976; Fudali, 1981; Barrat et al., 1997), where Al_2O_3, TiO_2, and FeO_{tot} are found in few percent abundances as well. The rare earth elements (REE) pattern and the light-REE (LREE) enrichment associated with a negative Eu anomaly are compatible with a post-Archean terrigenous source, probably an upper continental crust rock (e.g., a mature quartz-arenite, Barrat et al., 1997). Some compositionally layered specimens present dark portions that are enriched in siderophile elements such as Ni, Cr, Co, Ir, and platinum-group elements (Barrat et al., 1997; Cipriani et al., 2000; Murali et al., 1989; Rocchia et al., 1997), with chondritic Ni/Co, Fe/Ni, and Fe/Mg ratios; Os isotope ratios (Koeberl, 1997, 2000; Murali et al., 1997); and iron that is in the reduced, bivalent state (Giuli et al., 2003).

Microscopic inclusions are often found within the LDG glassy groundmass. Among these, there are several mineral and amorphous inclusions which record a high-temperature (>1670°C) event in the LDG formation. These include lechatelierite (Weeks et al., 1984), α-cristobalite (Cavosie et al., 2022), baddeleyite (Kleinmann, 1969), and mullite (Greshake et al., 2017). Lechatelierite is a natural fused, amorphous SiO_2 formed through quenching of silica melt at temperatures higher than 1700°C (Ferrière et al., 2009; Lacroix, 1915); α-cristobalite is the tetragonal polymorph of SiO_2 formed through displacive transformation at low temperature, usually below 270°C, from the high-temperature cubic β-cristobalite (Cavosie et al., 2022; Dollase, 1965); baddeleyite is monoclinic ZrO_2 which may derive from the reversion of the tetragonal zirconia at temperatures higher than 1676°C (Butterman & Foster, 1967); mullite is a high-temperature aluminosilicate derived from the decomposition of kaolinitic clays at temperatures higher than 1600°C (Greshake et al., 2017; Schneider & Komarneni, 2006). Pratesi et al. (2002) observed nanometric spherules of glass enriched in Mg, Al, and Fe in LDG and interpreted them as liquid immiscibility, setting a minimum formation temperature in the range of 1700°C–2100°C.

Recent studies of impact melt rocks, including LDG, found the presence of granular zircons that preserve crystallographic orientations inherited from the high-pressure polymorph reidite (Cavosie et al., 2018). These are called FRIGN (*former reidite in granular neoblastic*) zircons, and they would indicate pressures up to 30 GPa (Cavosie & Koeberl, 2019), which favor the direct impact hypothesis. However, Kovaleva et al. (2021) demonstrated that the granular neoblastic zircon may relate to disequilibrium melting and crystallization of zircons at high-temperature regimes, independently of pressure, although the feasibility of this process was questioned by Zhao et al. (2024). In addition, Kovaleva et al. (2023) found orthorhombic zirconia in LDG, a polymorph of ZrO_2 which is stable between 12.5 and 24.0 GPa (Liu, 1980). Shocked quartz has also been reported from rocks within the LDG field (Koeberl & Ferrière, 2019). Lastly, an FeNi silicide spherule was identified in LDG via combined neutron and X-ray tomography (Martell et al., 2024). The authors interpreted the latter evidence as projectile material incorporated in the LDG melt.

Despite the variety of available data, the origin of LDG is still enigmatic. Among the various hypotheses advanced so far, the most debated are the impact cratering and the airburst origin: the former supported by high-pressure evidence and impactor contamination, while the latter by the lack of an associated impact crater, which proves to be the most challenging problem when dealing with the origin of impact melt rocks. Since the late 1960s, several structures have been proposed as the source crater of LDG, for example, the BP impact crater and the Oasis impact structure (Martin, 1969; Reimold & Koeberl, 2014), but all of them were later discarded because of age, size, and composition of the target material (Saul, 2018; Schaaf & Müller-Sohnius, 2002). Another possible structure, Kebira, was later demonstrated to be of non-impact origin (Orti et al., 2008; Paillou et al., 2004, 2006). However, considering a moderate estimate of an average crater erosion rate for Northern Africa (30 m/*Ma*, Hergarten & Kenkmann, 2019), the potential impact crater could have been completely eroded over the last 29 *Ma*. Numerical simulations of impacts of stony and cometary bodies confirmed that the LDG strewn field could have formed either by impact cratering or an airburst (Svetsov et al., 2020).

The situation is further complicated by the fact that the parent material of LDG has not been conclusively identified yet, as LDG exhibits a different isotope composition than that of the rocks in the region where it is found (e.g., Schaaf & Müller-Sohnius, 2002). However, many workers agree with the idea that the parent material would be represented by mature Cretaceous sandstones derived from the erosion of intrusive igneous rocks of Pan-African (Neoproterozoic) age (e.g., Sighinolfi et al., 2020).

Considering the level of uncertainty of petrogenetic models based only on the analysis of the glass phase of

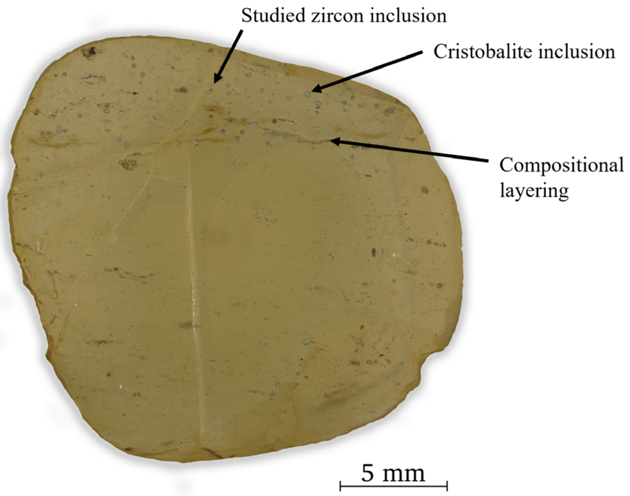

FIGURE 1. Stereomicrograph of the polished section labeled LDG24. The studied zircon, a cristobalite inclusion, and a dark band related to the compositional layering are arrowed. (Color figure can be viewed at wileyonlinelibrary.com)

LDG, the study of crystalline inclusions provides a valid alternative to put new constraints on the origin of LDG. Here, we report the first finding of a microscopic dendritic zircon inclusion inside LDG. The inclusion, studied down to the nanoscale, with novel electron microscopy and 3D electron diffraction (3DED) techniques (e.g., Gemmi et al., 2019; Gorelik et al., 2019), provides a new estimate of the peak temperature for the formation of LDG.

SAMPLES AND METHODS

The zircon inclusion studied here was found in a polished section of a specimen labeled LDG24 (found at 25° 17′ 05″ N, 25° 33′ 58″ E), kindly provided by Romano Serra, from the collection of the Museo del Cielo e della Terra in S. Giovanni in Persiceto (Bologna, Italy). The section shows the recurrent characteristic features, namely the bright yellow color, vitreous luster, and the compositional banding (Figure 1).

Preliminary electron imaging was performed with a JEOL JSM 6610-LV scanning electron microscope (SEM), with an accelerating voltage of 15 kV and variable beam current, at the Naturhistorisches Museum Vienna, Austria. Backscattered electron (BSE) imaging of the inclusion was performed using a Gemini II field emission gun-scanning electron microscope (FEG-SEM) of the Centre for Instrument Sharing of the University of Pisa (CISUP), under an acceleration voltage of 5 kV. The instrument is coupled with a Capella Focused Ion Beam (FIB) column with a Ga source which was used to cut an electron-transparent lamella following procedures described by Hyun Jung et al. (2012). Nanometer-scale analyses of the electron-transparent lamella were performed using a 200 kV JEOL JEM-F200 field-emission transmission electron microscope (FE-TEM) at CISUP. Imaging was performed in scanning-transmission electron microscopy (STEM) mode, using a high-angular annular dark field (HAADF) detector with low current on the specimen conditions (probe size 6 and condenser aperture 40 µm) not to damage the sample. Transmission electron microscopy energy-dispersive X-ray spectroscopy (TEM-EDS) analyses were acquired at a tilt angle of 15° using Cliff–Lorimer approximation (Cliff & Lorimer, 1975) and calibrated k-factors for the main chemical elements (Sanità et al., 2024). 3DED data were collected in STEM mode (nanodiffraction), using a camera length of 250 mm, a pseudo-parallel illumination obtained through the highest spot size (10), a condenser lens aperture of 10 µm, and a designated lens configuration. The probe beam diameter was approximately 30 nm. The total tilt range was from 60° to 120°. Diffraction pattern frames were collected at each 1° angle-tilt interval, with precession of the electron beam (precession semiangle 1°). Indexing of diffraction data was performed with PETS2 software (Palatinus et al., 2019) and unit cell parameters were compared with the reference material from RRUFF project (Lafuente et al., 2015).

Electron pair distribution functions (ePDFs) on the amorphous glasses were calculated from diffraction patterns recorded using a beam setting similar to that used for 3DED. The exposure of 60,000 ms and a camera length of 250 mm were used, corresponding to an effective pixel size of 0.0583 nm^{-1}. The diffraction data were stored as 24 bit gray scale image. The two-dimensional electron diffraction patterns were azimuthally integrated into one-dimensional intensity versus Q profiles using a custom MatLab script. To minimize the contribution of the primary, unscattered electron beam, the data were clipped in the low-Q region up to 0.4 $\mathring{A}^{-1}$. The remaining profile was normalized by the square of the combined SiO_2 atomic scattering amplitude profile. The residual background was modeled with a fourth-order polynomial. Before performing the Fourier transformation, the data were clipped to a maximum Q value Q_{max} of 9 $\mathring{A}^{-1}$. To suppress truncation ripples in the ePDF profiles, a 1/Q tapering function was applied to enforce asymptotic behavior at Q_{max}.

RESULTS

The zircon inclusion is located in the polished section labeled LDG24, in the region indicated by the arrows of Figure 1. This portion of the specimen is compositionally layered and contains abundant cristobalite inclusions that, in BSE images, appear similar to that reported in figure 3b of Cavosie et al. (2022).

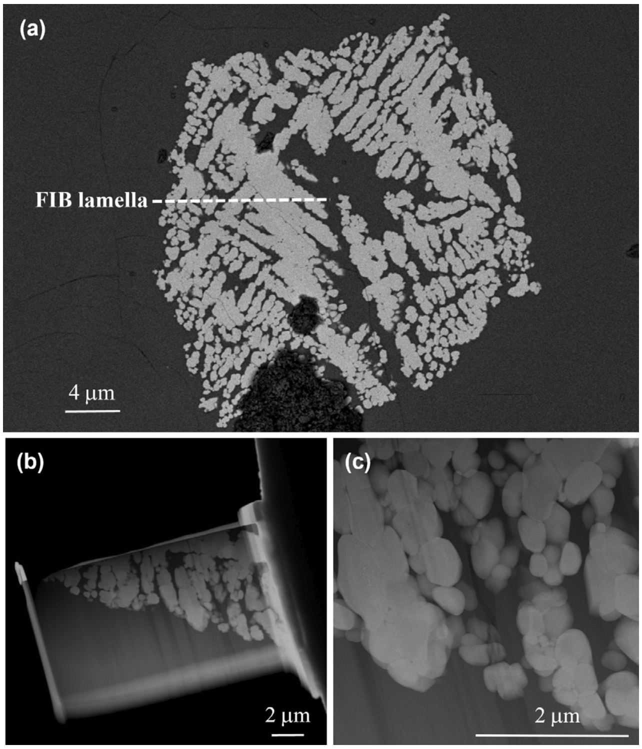

FIGURE 2. Electron microscope images of the studied zircon inclusion. (a) Backscattered electron (BSE) image of the inclusion. The dashed line indicates the location of the FIB lamella extracted for TEM studies. The dark object in the foreground is a dust speck. (b) Overview of the focused-ion beam (FIB) lamella in high-angular annular dark field scanning transmission electron microscopy (HAADF-STEM) mode. (c) Close-up showing zircon crystals in HAADF-STEM mode.

The zircon inclusion appears equant in shape, with similar 20 μm dimensions along all the axes (Figure 2a), and consists of dendritic branches composed of trails of submicroscopic zircon grains arranged in a reticulate–cruciform texture (Figure 2b,c). The interstices of the zircon branches are filled with glass (hereafter referred to as interstice-filling glass). An FIB lamella was prepared near the center of the inclusion (Figure 2a) that contains the zircon crystals, the LDG matrix, and the interstice-filling glass (Figure 2b,c).

Observations at the nanoscale were performed mainly in HAADF-STEM mode. However, a TEM bright-field (BF) image is reported in the Supporting Information (Figure S1). Imaging with HAADF-STEM mode shows that the submicroscopic zircon grains composing the dendritic branches have subhedral shapes (Figure 2c). No evidence of reaction with the surrounding glass, neither the LDG matrix nor the interstice-filling material, was observed.

Average element composition (in oxide wt%) results from STEM-EDS analyses are listed in Table 1.

TABLE 1. Element compositions (oxides wt%) of zircon crystals, LDG matrix, and interstice-filling glass obtained by STEM-EDS.

	Zircon		LDG matrix		Interstice-filling glass	
Oxide (wt%)	Average (n = 108)	σ	Average (n = 10)	σ	Average (n = 9)	σ
SiO_2	35.7	6.3	96.2	0.7	95.7	0.8
Al_2O_3	<0.5		0.8	0.2	1.0	0.2
Y_2O_3	1.0	0.6	n.d.		n.d.	
FeO	1.9	0.5	1.1	0.3	1.1	0.3
ZrO_2	59.5	6.3	1.8	0.6	2.1	0.7
HfO_2	1.5	0.6	<0.5		n.d.	
Total	100.0		100.0		100.0	

Abbreviations: *n*, number of spot analyses; n.d., not detected.

The average chemical formula of zircon, recalculated on the basis of four oxygen atoms, is $(Zr_{0.88}Y_{0.02}Fe_{0.05}Hf_{0.01})_{\Sigma 0.96}Si_{1.07}O_4$. The ZrO_2 and SiO_2 content in zircon crystals range from 43.9 wt% to 64.3 wt% and from 30.6 wt% to 52.5 wt%, respectively (see Table S1). In addition, some point analyses on zircon showed the presence of UO_2 and ThO_2 up to a maximum content of about 1.1 wt% and TiO_2 up to almost 0.2 wt%. Note that the chemical variability for SiO_2 and ZrO_2 may be related to different extents of contamination by the surrounding glass (i.e., the electron beam interaction volume may comprise some of the surrounding glass).

The LDG matrix and the interstice-filling glass are relatively similar in terms of EDS chemistry (Figure 3), although the interstice-filling glass is richer in Al_2O_3 and ZrO_2 relative to the LDG matrix. The difference in ZrO_2 content may be related, again, to contamination by the zircon grain. Glasses and zircon point analyses show a positive correlation in the SiO_2 versus Al_2O_3 plot, while in the SiO_2 versus ZrO_2 plot, they show a negative correlation. Single spot analyses of the LDG matrix and the interstice-filling glass are given in Table S2.

Decomposition products of zircon, such as baddeleyite or other ZrO_2 and SiO_2 polymorphs, and melt inclusions were not observed in HAADF-STEM imaging, and all the crystals analyzed with three-dimensional electron diffraction (3DED) were zircon (i.e., a = 6.6042, c = 5.9796 Å, V = 260.803 Å^3, space group $I4_1/amd$, Hazen & Finger, 1979). Table 2 lists the cell parameters obtained after PETS2 data elaboration. The average value of the c parameter is about 6.017 Å, which is off 0.037 Å with respect to the standard value of Hazen and Finger (1979). Such deviation is a 0.6% difference which is considered inside the error for the technique. However, as shown by Table S1, some slight compositional differences among

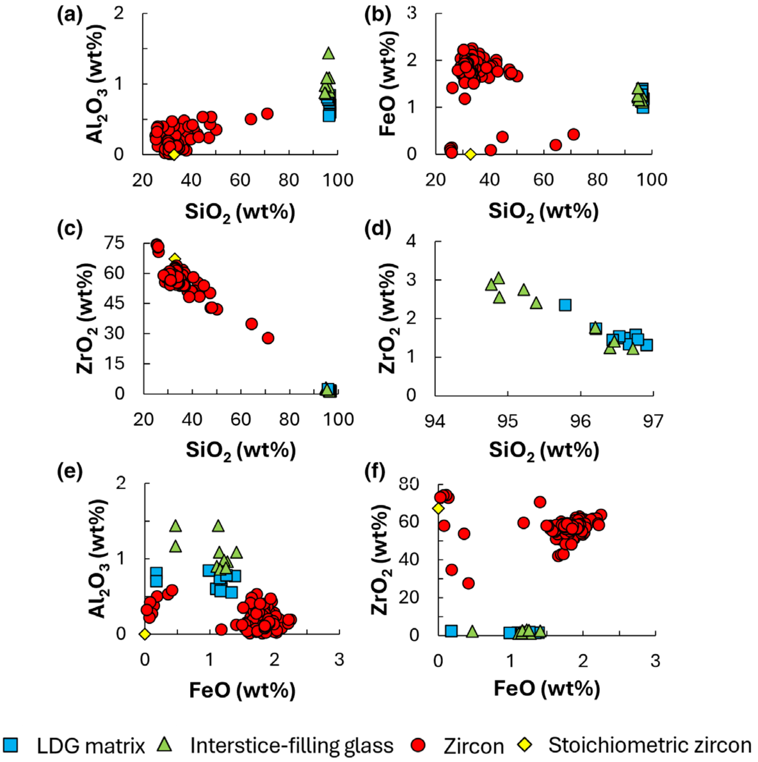

FIGURE 3. Major element variation diagrams of the studied zircon and host glass. Concentrations are in oxide wt% and determined through energy-dispersive X-ray spectroscopic analyses. Red circles represent zircon crystals, blue squares represent the LDG matrix, green triangles indicate the interstice-filling glass, and yellow diamond indicates the composition on the diagram of stoichiometric zircon. (a) SiO_2 versus Al_2O_3. (b) SiO_2 versus FeO. (c) SiO_2 versus ZrO_2. (d) Enlarged section of SiO_2 versus ZrO_2 showing the 94–97 wt% range. (e) FeO versus Al_2O_3. (f) FeO versus ZrO_2. (Color figure can be viewed at wileyonlinelibrary.com)

TABLE 2. Cell parameters obtained via three-dimensional electron diffraction on selected positions of crystals.

Point	*a* (Å)	*c* (Å)	*V* (Å^3)
1	6.656 (5)	6.014 (5)	266.4 (6)
2	6.656 (5)	6.004 (5)	266.0 (6)
3	6.646 (3)	6.015 (3)	266.0 (9)
4	6.643 (6)	6.007 (7)	265.1 (8)
5	6.660 (4)	5.987 (5)	265.6 (5)
6	6.648 (4)	6.012 (4)	265.7 (5)
7	6.641 (2)	6.026 (2)	265.8 (2)
8	6.654 (2)	6.018 (2)	266.5 (2)
9	6.646 (3)	6.031 (4)	266.4 (4)
10	6.629 (4)	6.006 (5)	263.9 (5)
11	6.721 (4)	6.090 (5)	275.1 (6)
12	6.662 (4)	6.028 (4)	267.5 (5)
13	6.645 (4)	6.008 (6)	265.3 (6)

individual crystals, as well as inside the same crystal, are present. These differences may account for little variation in cell parameters.

Several long-exposure electron diffraction patterns were collected in the interstice-filling glass and the LDG matrix. These patterns present concentric broad rings, characteristic of amorphous materials. The diffraction data were azimuthally integrated, normalized, and processed to determine an electron pair distribution function (ePDF), revealing structural differences between the LDG matrix and the interstice-filling glass. Analysis of a representative pair of patterns is reported in Figure 4. Figure 4a shows the original electron scattering profiles for electron diffraction patterns recorded from two distinct areas. Figure 4b displays the sample profiles after normalization and background subtraction (named F(Q)). The F(Q) profiles were used to calculate the final ePDFs. Even in the F(Q), a slight shift of the structural peaks between the two types of materials can be observed (red and blue curve in Figure 4b). The scattering curve was recorded only up to a Q slightly above 8, and therefore, the ePDF was calculated with a Qmax of 8.3 Å^{-1}. The ePDF (Figure 4c) reveals structural oscillations up to 8 Å, suggesting that the structural order domains are approximately 8 Å in diameter. The position of the first peak, that is the one located at ~1.6 Å, corresponds to the direct Si-O distance (i.e., the bond length), while the second peak, located at ~2.7 Å,

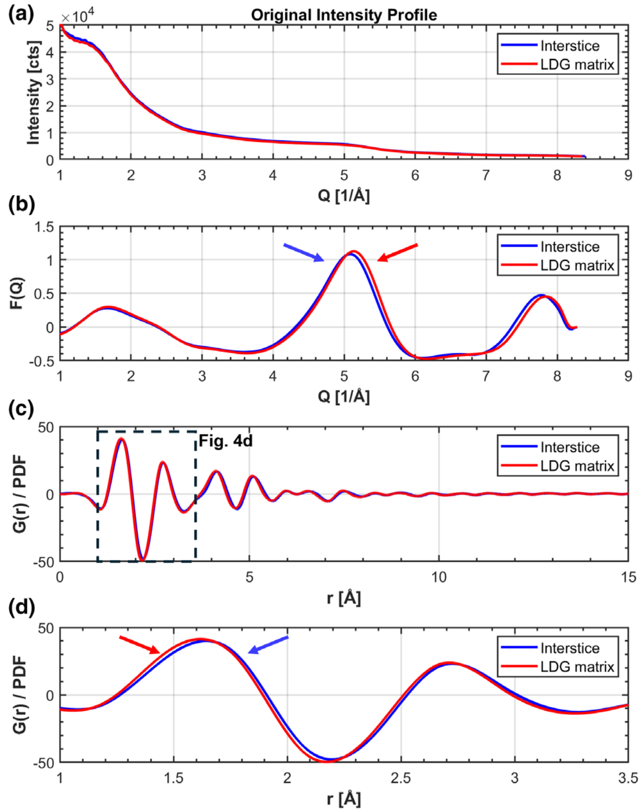

FIGURE 4. Electron pair distribution function analysis of the interstice-filling glass (blue) and LDG matrix (red). (a) Original intensity profile. (b) Final profile after background subtraction and normalization (F(Q)), used for electron pair distribution function calculation. (c) G(r)–electron pair distribution functions (ePDFs). The dashed rectangle indicates the position of Figure 4d. (d) Enlarged section of G(r) highlighting the peak shift. [Correction added on 27 January 2026, after first online publication: Figure 4 has been updated in this version.] (Color figure can be viewed at wileyonlinelibrary.com)

represents the O-O distance in an SiO_4 tetrahedron. Despite keeping the same electron diffraction parameters, a slight shift in peak positions of the first and second peak of the ePDF was observed (Figure 4d). For the LDG matrix, the Si-O peak occurs at 1.57–1.60 Å, whereas in the interstice-filling glass, it is slightly broader, at 1.62–1.64 Å. A similar shift is observed for the O-O distance: 2.69–2.70 Å in the LDG matrix and 2.71–2.73 Å in the interstice-filling glass.

While the absolute values of the distances are directly related to the systematic error in the electron diffraction camera length calibration and should therefore be treated with caution, the relative shift is evident.

DISCUSSION

The dendritic habit of the zircon inclusion presented in this work is novel for LDG. No dendritic grains were reported in the largest and most systematic study of zircon crystals ($n = 101$) in LDG (Cavosie & Koeberl, 2019). However, dendritic zircon has been reported in other impact-related materials as well as in some terrestrial rocks (e.g., Corfu et al., 2003). Dendritic zircon was found, for example, in some glass fragments of the Logoisk structure and interpreted as the result of zircon decomposition during quench of the impact melt (Glazovskaya et al., 2024).

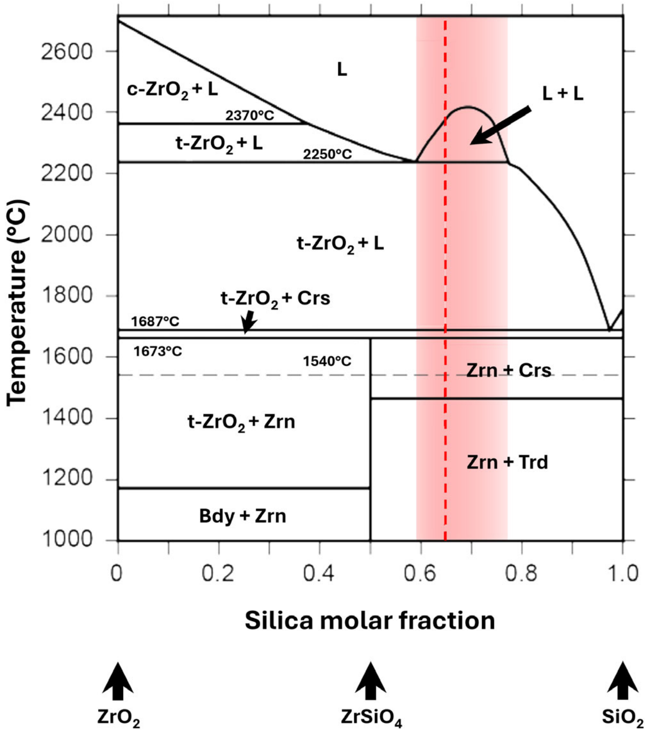

FIGURE 5. Phase diagram for the ZrO_2-SiO_2 system (modified after Telle et al., 2015). The red dashed line indicates the composition of our system from image analysis and EDS data, the pink shaded region indicates the compositions for which a temperature higher than 2250°C leads the system over liquidus. The relative abundance of phases was estimated by image analysis of a cropped region of Figure 2 that encloses the zircon inclusion and the interstice-filling glass only and gave 65% SiO_2–35% ZrO_2 as composition of the system. The horizontal dashed gray line indicates a lower dissociation temperature defect-related (Curtis & Sowman, 1953). Abbreviations follow the official IMA-CNMNC approved symbols (Warr, 2021) and are Zrn for zircon, Bdy for baddeleyite, Crs for cristobalite, and Trd for tridymite. (Color figure can be viewed at wileyonlinelibrary.com)

Examples of dendritic zircon in terrestrial rocks include volcaniclastic rocks from southwest China (Wang et al., 2022), mafic rocks of the Skaergaard intrusion (Moerhuis et al., 2025), metasomatized nordmakites from the Mongolian Altai (Kempe et al., 1999), and peralkaline granites from the Ambohimirahavavy alkaline complex (Estrade et al., 2014). In the first case, the lack of any correlation between zircon morphology and the mineral assemblage in which the zircon is found led the authors to propose that zircon morphology is independent of melt chemistry. In turn, Kempe et al. (1999) and Estrade et al. (2014) interpreted the anomalous abundance of Fe, Ca, U, Th, Y, and REE in dendritic zircon as due to secondary and hydrothermal processes. While dendritic textures are indicative of a dynamic crystallization mechanism, the incorporation of incompatible elements is typically ascribed to conditions indicating thermodynamic disequilibrium (e.g., MacDonald et al., 2022).

In the case of the zircon inclusion examined in this study (Figure 2), the nearly orthogonal arrangement of the dendritic branches points to a rapid growth of the individual grains, which is consistent with a diffusion-limited growth mechanism driven by the high supersaturation of the mineral phase in the melt (see e.g., Arzilli et al., 2022; Colle et al., 2023). This mechanism, however, requires the initial presence of an immiscible liquid droplet, likely of the same mass and composition of the inclusion, that eventually crystallized under a regime of high undercooling during the post-shock cooling of the LDG melt.

The composition of the interstice-filling glass, which deviates from the composition of the LDG glass matrix (e.g., in the Al_2O_3 versus FeO variation diagram, Figure 3), provides further evidence for a diffusion-limited growth mechanism of the zircon under a regime of high undercooling, as it may represent the diffusive boundary layer derived from the rapid crystallization of the zircon. In a similar fashion, the abundance of trace elements such as U, Th, Hf, and Ti in the dendritic zircon could be an indicator that it crystallized very rapidly, as also proposed by Moerhuis et al. (2025) in their study of dendritic zircon in the Skaergaard intrusion rocks.

It is well known that LDG is a material formed under disequilibrium conditions, as documented by the occurrence of compositional banding and partially decomposed mineral inclusions (e.g., Kleinmann, 1969; Pratesi et al., 2002). Thus, it is reasonable to assume that the zircon inclusion examined in this study formed by incipient melting of a precursor zircon grain and subsequent crystallization while the LDG was still in a molten state, following the LDG-forming event, either impact cratering or an airburst. Likewise, the liquid formed by the precursor zircon grain (or grain aggregates) did not disperse into the silica-rich melt of the LDG nor did other mineral phases predicted in the ZrO_2-SiO_2 phase diagram formed (Figure 5). At the same time, although previous studies on zircon in LDG described dissociation to zirconia (Cavosie & Koeberl, 2019), a ZrO_2 phase that would be expected to form by incongruent melting of the precursor zircon during the heating stage is not observed in this work. This evidence may be ascribed to the conditions during which this specific sample of LDG formed. One possibility is that the precursor zircon transformed directly into an amorphous liquid phase. In fact, for strain rates higher than 10^7 s^{-1}, laser-driven shock experiments coupled with in situ X-ray diffraction showed that zircon does not decompose to SiO_2 and ZrO_2, but rather transforms into an amorphous liquid (Takagi et al., 2022). Typical shock strain rates are even much more severe than the ones reported by Takagi et al. (2022), in the range between 10^4 and 10^6 s^{-1} (Grieve, 1991) and very far from the endogenous conditions (about 10^{14} s^{-1}, Kenkmann et al., 2014). Alternatively, intermediate compounds may have formed by incongruent melting of the precursor zircon but not have survived upon further increase in temperature.

In this second case, clues on the peak temperature experienced by the LDG can be obtained by some simple considerations on the ZrO_2-SiO_2 phase diagram (Telle et al., 2015, Figure 5). From a chemical point of view, if the parent zircon is assumed to be non-metamict, then a certain amount of mixing of the liquid produced during the melting of the zircon with the silica-rich LDG melt must be invoked to explain the compositional variability of the interstice-filling glass. It should be noted that, although the non-metamict nature of the zircon inclusion cannot be known unequivocally, the high abundance of trace elements (Table 1) suggests that the parent zircon may have been metamict to some extent, thus having different thermodynamical properties, namely the melting temperature.

We calculated the bulk chemical composition of the inclusion based on the average chemical composition of the zircon crystals and the interstice-filling glass (Table 1), using the relative abundance of these two constituents. Assuming negligible chemical exchange with surrounding LDG groundmass, such relative abundance was determined by image analysis with ImageJ (Schneider et al., 2012), which gave a zircon–glass ratio of 0.54:0.46. By multiplying these fractions for the average zircon and interstice-filling glass chemical composition, we obtained the percentage of SiO_2 and ZrO_2 in the zircon and glass in that portion of LDG, respectively. The relative fraction of SiO_2 and ZrO_2 over the sum $SiO_2 + ZrO_2$ led to the 65% SiO_2–35% ZrO_2 composition used in the phase diagram (Figure 5).

Based on the information derived from the phase diagram note, a field of immiscibility opens when the temperature increases above 2250°C. Under such conditions, the dissolution of the liquid forming the inclusion into the silica-rich LDG melt was likely inhibited and, in turn, the crystallization kinetics during the cooling of the system determined the crystallization of dendritic zircon while suppressing other ZrO_2 phases.

The ePDF data presented here show that the interstice-filling glass appears to be more relaxed in terms of Si-O bonds relative to the LDG glass matrix. For crystalline phases, Si-O bond lengths vary across different silica polymorphs, such as quartz (1.59–1.62 Å, e.g., Kihara, 1990; Wei, 1935; Wyckoff, 1926), tridymite (1.56–1.60 Å, Dollase, 1967; Graetsch, 2001; Hirose et al., 2005), cristobalite (1.60–1.61 Å, Dollase, 1965; Peacor, 1973; Pluth et al., 1985), and coesite (1.60–1.61 Å, Angel et al., 2003; Levien & Prewitt, 1981). The Si-O bond distance observed in the LDG matrix corresponds to the lower limit of those crystalline phases, while the interstice-filling glass is in excess with respect to this limit (within the accuracy of the electron diffraction measurements mentioned above).

According to our model, the interstice-filling glass is intimately associated with the formation of the zircon inclusion from the immiscible liquid droplet and underwent the same thermal history. We believe that this interstitial glass solidified after the crystallization of the dendritic zircon, thereby explaining its chemical composition enriched in ZrO_2 (~2 wt%) and Al_2O_3 (~1 wt%), as determined by TEM-EDS analyses (Table 1). While the relative high concentration in ZrO_2 can be explained by the incomplete crystallization of the zircon melt derived from the melting of the precursor grain (or grain aggregate), the higher abundance of Al_2O_3 is explained by the incompatibility of Al in the zircon structure and subsequent concentration at the melt interface. However, if the parent zircon grain was metamict, Al could be derived from it during recrystallization. The higher degree of relaxation of the interstice-filling glass compared to the glass matrix of the LDG may be related either to a relaxation upon shock unloading in an impact cratering context or, more likely, to an effect of the relatively high concentration of Al_2O_3 in the interstitial melt, which lengthens the tetrahedron bonds.

In Figure 6, we propose a model for the formation of the dendritic zircon in LDG observed in this study. Our idea is that our LDG specimen samples a portion of the LDG precursor material consisting of quartz grains containing inclusions of, or mixed with, microscopic grains of zircon. This is in agreement with the current idea that the LDG precursor material was either a mature Cretaceous sandstone or its loose sediment degradation products derived from the erosion of Neoproterozoic intrusive igneous rocks (Sighinolfi et al., 2020). This material was subjected to a shock wave and during and after the shock unloading, post-shock temperatures reached very high values which brought the system above the liquidus of the ZrO_2-SiO_2 system, namely above 2250°C for composition between ~58% and ~78% SiO_2 (which is the case of our system). Under such conditions, all the system would be in a molten state and the immiscibility would have limited the dissolution of the liquid droplet produced by the melting of the zircon. The rapid cooling of this liquid would have led to the dynamic crystallization of zircon with a reticulate–cruciform texture, while kinetically suppressing the formation of other phases expected from the ZrO_2-SiO_2 phase diagram. The newly crystallized zircon would have taken most of the ZrO_2 and part of SiO_2 of the melt, rejecting incompatible components (such as Al_2O_3) that were consequently concentrated in the melt. As a result, the interstitial glass became enriched in Al_2O_3, which explains the distances of tetrahedral oxygen retrieved by ePDF data. Alternatively, it may be possible that, during crystallization, the zircon adsorbed some of the silica present in the surrounding melt matrix. Then, the latter would have been Al-enriched compared to the LDG matrix glass.

The disequilibrium conditions of LDG formation are supported by the occurrence of compositional banding and partially decomposed mineral inclusions (e.g., Cavosie et al., 2022; Kleinmann, 1969; Pratesi et al., 2002). We believe that the crystallization of the zircon inclusion reported in this work is a process that occurred very rapidly, far from the thermodynamic equilibrium, that is, it is a kinetic rather than thermodynamic controlled process. The velocity of such crystallization was such that no intermediate phase such as zirconia and silica polymorphs (Kleinmann, 1969; Kovaleva et al., 2023) crystallized from the parent zircon during the cooling path of the system. This idea is supported by the fact that the incipient melting of zircon is considered an indicator of post-shock temperatures higher than 2000°C, as suggested by Hamann et al. (2016). In their impact experiments (two-stage light-gas gun) on a quartz sand target with accessory microscopic zircon grains, Hamann et al. (2016) show that a "zircon-melt" immersed in a silica matrix composed of both quartz and lechatelierite formed (see their figure 12a). The authors invoked pressure and temperature amplifications associated with the pore collapse process in the porous target used in their shock recovery experiments to account for the observed incipient melting of quartz and zircon along grain boundaries.

The high temperature in excess of 2050°C recorded by the dendritic zircon studied here could also be the result of localized temperature excursion due, for instance, to pore collapse. However, since no other dendritic zircon has been found in the extensive survey conducted by Cavosie and Koeberl (2019) on seven other specimens, it is also possible that our LDG specimen does sample a higher temperature impact melt batch. The latter possibility should be checked through careful investigation of other specimens.

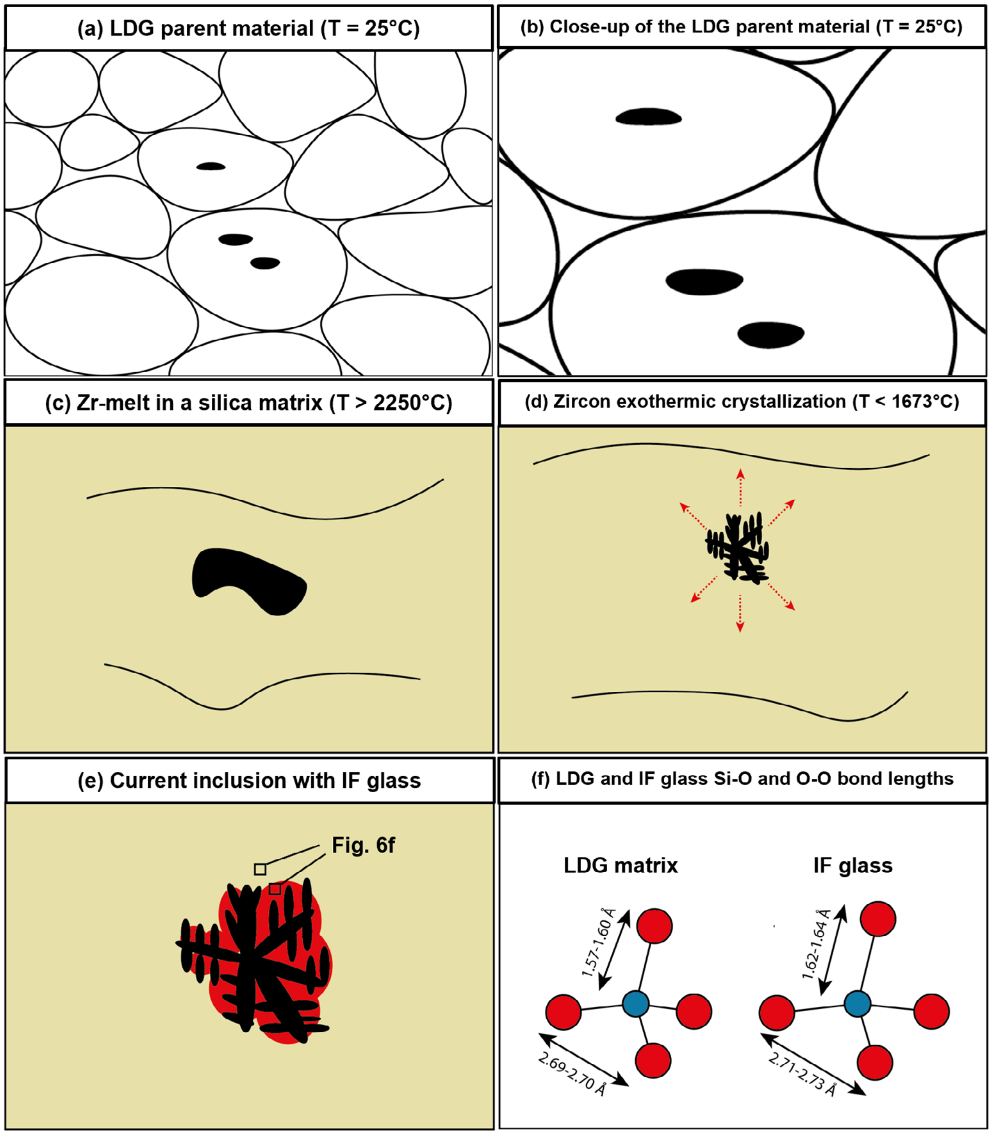

FIGURE 6. Schematic model for the formation of the dendritic zircon studied in this work. (a) Libyan Desert Glass (LDG) parent material at ambient temperature, before the LDG-forming event. White ellipses represent quartz grains; black ellipses indicate zircon grains. The temperature T is 25°C. (b) Close-up of the LDG parent material shown in Figure 6a, showing quartz grains (white ellipses) and zircon grains (black ellipses). (c) Zirconium-melt (black pocket) immersed in a melt which results from the mixing of the Si melt derived from the incipient melting of the zircon grains and the LDG melt. (d) Very fast crystallization of zircon in disequilibrium conditions, which leads to a dendritic structure (black ellipses) and absence of intermediate ZrO_2 and SiO_2 phases. Red dashed lines indicate the rejection of Al from the zircon structure. (e) Current state of the dendritic zircon inclusion. The red area surrounding some stems and arms of the dendritic zircon represents the interstice-filling glass (IF in the image text). (f) Schematic representation of the TO_4 tetrahedron (in this case, we assume T = Si) for the LDG matrix (left) and the IF glass (right), showing the different bond length values. Blue dots represent silicon atoms; red dots represent the oxygen atoms. [Correction added on 27 January 2026, after first online publication: Figure 6 has been updated in this version.] (Color figure can be viewed at wileyonlinelibrary.com)

The thermal regime recorded by the dendritic zircon studied here is, however, in good agreement with the temperatures inferred from numerical simulations (Svetsov et al., 2020), which showed that, for different types of projectiles and entry angles and speeds, the impact melting of the LDG parent material occurred at temperatures higher than 2000°C. Svetsov et al. (2020) proposed that such temperatures and the formation of LDG could be achieved during an airburst involving either a stony body (3.3 g/cm^3 density) with a diameter of 300 m, an entry speed of 35 km/s, and an entry angle of 8° or an icy (1 g/cm^3 density) body with diameters of 300, 200, and 150 m and entry speeds of 50, 70, and 70 km/s and entry angles of 15°, 30°, and 45°, respectively.

Svetsov et al. (2020) also showed that such thermal regimes could be alternatively reached through the direct impact onto the Earth's crust of a stony projectile with a diameter of 300 m, an entry speed of 20 km/s, and an entry angle of 15°.

Our results, especially the temperature reached by the chemical system and the kinetics of heating/cooling rates, seem to fit well in an impact melting scenario, where disequilibrium conditions prevail. This work alone is unable to discriminate effectively if the LDG truly formed as a consequence of impact melting during impact cratering or during an airburst, for example, due to the lack of high-pressure evidence. However, it adds information regarding the conditions and mechanisms affecting minerals at the extreme thermal conditions under which the LDG formed.

CONCLUSIONS

The studied zircon inclusion represents the first finding of a skeletal dendritic texture in zircon within LDG. Textural evidence, chemical data, and absence of intermediate ZrO_2 and SiO_2 phases suggest that the zircon grain crystallized very rapidly from a liquid droplet formed by impact melting of a zircon grain (or grains aggregate), embedded in a quartz-dominated precursor material, partially mixed with the LDG melt. Crystallization occurred in conditions very far from thermodynamic equilibrium, as testified by the suppression of mineral phases that are expected from the ZrO_2-SiO_2 phase diagram. Our hypothesis is that the chemical system (zircon and LDG precursor rock, roughly in a ratio 2:1) reached a high temperature above the liquidus, namely above 2250°C, and directly transformed zircon into a melt. The preservation of the inclusion was possible because of the immiscibility between the liquid droplet from which the zircon inclusion formed and the LDG liquid. The disequilibrium crystallization of the zircon is attested by the exceptional abundance of trace elements in zircon and the higher concentration of incompatible components in the interstice-filling glass.

Acknowledgments—This work is part of the MSc thesis of NM conducted at the Dipartimento di Scienze della Terra of the University of Pisa. NM acknowledges support from the ERASMUS programme for his research visit at the Naturhistorisches Museum Wien, Vienna, Austria. The authors acknowledge the support of the Centre for Instrument Sharing of the University of Pisa (CISUP) and Dr. Romano Serra for providing the studied specimen. The authors acknowledge E. Kovaleva, T. M. Erickson, and A. J. Cavosie for their constructive reviews and C. Koeberl for editorial handling. Planetary material research at the University of Pisa is carried out with the support of the Space It Up project funded by the Italian Ministry of the University and Research (MUR) and the Agenzia Spaziale Italiana (ASI)—Contract n. 2024-5-E.0—CUP n. I53D24000060005. Open access publishing facilitated by Universita degli Studi di Milano-Bicocca, as part of the Wiley - CRUI-CARE agreement.

Data Availability Statement—The data that support the findings of this study are available from the corresponding author upon reasonable request.

Editorial Handling—Dr. A. J. Timothy Jull

REFERENCES

Angel, R. J., Shaw, C. S. J., and Gibbs, G. V. 2003. Compression Mechanism of Coesite. *Physics and Chemistry of Minerals* 30: 167–176. https://doi.org/10.1007/s00269-003-0303-9.

Arzilli, F., Polacci, M., La Spina, G., Le Gall, N., Llewellin, E. W., Brooker, R. A., Torres-Orozco, R., et al. 2022. Dendritic Crystallization in Hydrous Basaltic Magmas Controls Magma Mobility within the Earth's Crust. *Nature Communications* 13: 1–14. https://doi.org/10.1038/s41467-022-30890-8.

Barnes, V. E., and Underwood, J. R. 1976. New Investigations of the Strewn Field of Libyan Desert Glass and its Petrography. *Earth and Planetary Science Letters* 30: 117–122. https://doi.org/10.1016/0012-821X(76)90013-3.

Barrat, J. A., Jahn, B. M., Amossé, J., Rocchia, R., Keller, F., Poupeau, G. R., and Diemer, E. 1997. Geochemistry and Origin of Libyan Desert Glasses. *Geochimica et Cosmochimica Acta* 61: 1953–59. https://doi.org/10.1016/S0016-7037(97)00063-X.

Bigazzi, G., and De Michele, V. 1996. New Fission-Track Age Determination of Impact Glasses. *Meteoritics & Planetary Science* 31: 234–36. https://doi.org/10.1111/j.1945-5100.1996.tb02017.x.

Butterman, W. C., and Foster, W. R. 1967. Zircon Stability and the ZrO_2-SiO_2 Phase Diagram. *American Mineralogist* 52: 880–85.

Cavosie, A., and Koeberl, C. 2019. Overestimation of Threat from 100 Mt-Class Airburst? High-Pressure Evidence from Zircon in Libyan Desert Glass. *Geology* 47: 609–612. https://doi.org/10.1130/G45974.1.

Cavosie, A. J., Rickard, W. D. A., Evans, N. J., Rankeburg, K., Roberts, M., Macris, C. A., and Koeberl, C. 2022. Origin of β-Cristobalite in Libyan Desert Glass: The Hottest Naturally Occurring Silica Polymorphism? *American Mineralogist* 107: 1325–40. https://doi.org/10.2138/am-2021-7922.

Cavosie, A. J., Timms, N. E., Ferrière, L., and Rochette, P. 2018. FRIGN Zircon—The Only Terrestrial Mineral Diagnostic of High-Pressure and High-Temperature Shock Deformation. *Geology* 46: 891–94. https://doi.org/10.1130/G45079.1.

Cipriani, C., Corzza, M., Giuli, M., Cecchi, V. M., Pratesi, G., Rossi, P., and Vittone, E. 2000. Ion Beam Study of a Possible Extraterrestrial Body Signature in Libyan Desert Glass. *Nuclear Instruments and Methods in Physics Research* 170: 187–192.

Clayton, P. A., and Spencer, L. J. 1933. Silica-Glass from the Libyan Desert. *Mineralogical Magazine* 23: 501–8.

Cliff, G., and Lorimer, G. W. 1975. The Quantitative Analysis of Thin Specimens. *Journal of Microscopy* 103: 203–7. https://doi.org/10.1111/j.1365-2818.1975.tb03895.x.

Colle, F., Masotta, M., Costa, S., Mollo, S., Landi, P., Pontesilli, A., Peres, S., and Mancini, L. 2023. Effect of Undercooling on Clinopyroxene Crystallization in High K Basalt: Implications for Magma Dynamics at Stromboli Volcano. *Lithos* 456-457: 107327. https://doi.org/10.1016/j.lithos.2023.107327.

Corfu, F., Hanchar, J. M., Hoskin, P. W. O., and Kinny, P. 2003. Atlas of Zircon Textures. *Reviews in Mineralogy and Geochemistry* 53: 469–500. https://doi.org/10.2113/0530469.

Curtis, C. E., and Sowman, H. G. 1953. Investigation of the Thermal Dissociation, Reassociation, and Synthesis of Zircon. *Journal of the American Ceramic Society* 36: 190–98. https://doi.org/10.1111/j.1151-2916.1953.tb12865.x.

Dollase, W. A. 1965. Reinvestigation of the Structure of Low Cristobalite. *Zeitschrift für Kristallographie* 121: 369–377. https://doi.org/10.1524/zkri.1965.121.16.369.

Dollase, W. A. 1967. The Crystal Structure at 220°C of Orthorhombic High Tridymite from the Steinbach Meteorite. *Acta Cristallographica* 23: 617–623. https://doi.org/10.1107/S0365110X67003287.

Estrade, G., Salvi, S., Béziat, D., Rakotovao, S., and Rakotondrazafy, R. 2014. REE and HFSE Mineralization in Peralkaline Granites of the Ambohimirahavavy Alkaline Complex, Ampasindava Peninsula, Madagascar. *Journal of African Earth Sciences* 94: 141–155. https://doi.org/10.1016/j.jafrearsci.2013.06.008.

Ferrière, L., Koeberl, C., and Reimold, W. U. 2009. Characterisation of Ballen Quartz and Cristobalite in Impact Breccias: New Observations and Constraints on Ballen Formation. *European Journal of Mineralogy* 21: 203–217. https://doi.org/10.1127/0935-1221/2009/0021-1898.

Fröhlich, F., Poupeau, G., Badou, A., Le Bourdonnec, F. X., Saquin, Y., Dubernet, S., Bardintzeff, J. M., Véran, M., Smith, D. C., and Diemer, E. 2013. Libyan Desert Glass: New Field and Fourier Transform Infrared Data. *Meteoritics and Planetary Science* 48: 2517–30. https://doi.org/10.1111/maps.12223.

Fudali, R. F. 1981. The Major Element Chemistry of Libyan Desert Glass and the Mineralogy of its Precursor. *Meteoritics* 16: 247–259. https://doi.org/10.1111/j.1945-5100.1981.tb00549.x.

Gemmi, M., Mugnaioli, E., Gorelik, T. E., Kolb, U., Palatinus, L., Boullay, P., Hovmöller, S., and Abrahams, J. P. 2019. 3D Electron Diffraction: The Nanocrystallography Revolution. *ACS Central Science* 5: 1315–29. https://doi.org/10.1021/acscentsci.9b00394.

Giuli, G., Paris, E., Pratesi, G., Koeberl, C., and Cipriani, C. 2003. Iron Oxidation State in the Fe-Rich Layer and Silica Matrix of Libyan Desert Glass: A High-Resolution XANES Study. *Meteoritics and Planetary Science* 38: 1181–86. https://doi.org/10.1111/j.1945-5100.2003.tb00306.x.

Glazovskaya, L. I., Shcherbakov, V. D., and Piryazev, A. A. 2024. Logoisk Impact Structure, Belarus: Shock Transformation of Zircon. *Meteoritics and Planetary Science* 59: 88–104. https://doi.org/10.1111/maps.14110.

Gorelik, T. E., Neder, R., Terban, M. W., Lee, Z., Mu, X., Jung, C., Jacob, T., and Kaiser, U. 2019. Towards Quantitative Treatment of Electron Pair Distribution Function. *Acta Crystallographica B* 75: 532–549. https://doi.org/10.1107/S205252061900670X.

Graetsch, H. 2001. X-Ray Powder Diffraction Study on the Modulated High Temperature Forms of SiO_2 Tridymite between 110 and 220°C. *Physics and Chemistry of Minerals* 28: 313–321. https://doi.org/10.1007/s002690100160.

Greshake, A., Wirth, R., Fritz, J., Jakubowski, T., and Böttger, U. 2017. Mullite in Libyan Desert Glass: Evidence for High-Temperature/Low-Pressure Formation. *Meteoritics & Planetary Science* 53: 467–481. https://doi.org/10.1111/maps.13030.

Grieve, R. A. F. 1991. Terrestrial impact: The record in the rocks. *Meteoritics* 26: 175–194. https://doi.org/10.1111/j.1945-5100.1991.tb01038.x.

Hamann, C., Stöffler, D., and Reimold, W. U. 2016. Interaction of Aluminum Projectiles with Quartz Sand in Impact Experiments: Formation of Khatyrkite ($CuAl_2$) and Reduction of SiO_2 to Si. *Geochimica et Cosmochimica Acta* 192: 295–317. https://doi.org/10.1016/j.gca.2016.07.018.

Hazen, R. M., and Finger, L. W. 1979. Crystal Structure and Compressibility of Zircon at High Pressure. *American Mineralogist* 64: 196–201.

Hergarten, S., and Kenkmann, T. 2019. Long-Term Erosion Rates as a Function of Climate Derived from the Impact Crater Inventory. *Earth Surface Dynamics* 7: 459–473. https://doi.org/10.5194/esurf-7-459-2019.

Hirose, T., Kihara, K., Okuno, M., Fujinami, S., and Shinoda, K. 2005. X-Ray, DTA and Raman Studies of Monoclinic Tridymite and its Higher Temperature Orthorhombic Modification with Varying Temperature. *Journal of Mineralogical and Petrological Sciences* 100: 55–69. https://doi.org/10.2465/jmps.100.55.

Hyun Jung, K., Sang, C. H., Hyung-Bin, B., and Tae Woo, L. 2012. Transmission Electron Microscopy (TEM) Sample Preparation of $Si_{1-x}Ge_x$ in *c*-Plane Sapphire Substrate. NASA/TM-2012-217597, 1–39.

Kempe, U., Götze, J., Dandar, S., and Habermann, D. 1999. Magmatic and Metasomatic Processes during Formation of the Nb-Zr-REE Deposits Khaldzan Buregte and Tsakhir (Mongolian Altai): Indications from a Combined CL-SEM Study. *Mineralogical Magazine* 63: 165–177. https://doi.org/10.1180/002646199548402.

Kenkmann, T., Poelchau, M. H., and Wulf, G. 2014. Structural Geology of Impact Craters. *Journal of Structural Geology* 62: 156–182. https://doi.org/10.1016/j.jsg.2014.01.015.

Kihara, K. 1990. An X-Ray Study of the Temperature Dependence of the Quartz Structure. *European Journal of Mineralogy* 2: 63–77. https://doi.org/10.1127/ejm/2/1/0063.

Kleinmann, B. 1969. The Breakdown of Zircon Observed in Libyan Desert Glass as Evidence of its Impact Origin. *Earth and Planetary Science Letters* 5: 497–501.

Klitzsch, E. 1978. Geologische Bearbeitung Südwest Ägyptens. *Geologische Rundschau* 67: 509–520. https://doi.org/10.1007/BF01802801.

Koeberl, C. 1997. Libyan Desert Glass: Geochemical Composition and Origin. In *Proceedings of the Silica '96 Meeting on Libyan Desert Glass and Related Desert Events*, edited by V. De Michele, 121–131. Milan: Pyramids.

Koeberl, C. 2000. Confirmation of a Meteoritic Component in Libyan Desert Glass from Osmium Isotope Data (Abstract #5253). *Meteoritcs & Planetary Science* 35: A89.

Koeberl, C., and Ferrière, L. 2019. Libyan Desert Glass Area in Western Egypt: Shocked Quartz in Bedrock Points to a Possible Deeply Eroded Impact Structure in the Region. *Meteoritics and Planetary Science* 54: 2398–2408. https://doi.org/10.1111/maps.13250.

Kovaleva, E., Helmy, H., Belkacim, S., Schreiber, A., Wilke, F. D. H., and Wirth, R. 2023. Libyan Desert Glass: New Evidence for an Extremely High-Pressure Temperature Impact Event from Nanostructural Study. *American Mineralogist* 108: 1906–23. https://doi.org/10.2138/am-2022-8759.

Kovaleva, E., Kusiak, M. A., Kenny, G. G., Whitehouse, M. J., Habler, G., Schreiber, A., and Wirth, R. 2021. Nano-Scale Investigation of Granular Neoblastic Zircon, Vredefort Impact Structure, South Africa: Evidence for Complete Shock Melting. *Earth and Planetary Science Letters* 565: 1–15. https://doi.org/10.1016/j.epsl.2021.116948.

Lacroix, F. 1915. La silice foudre considerée comme minéral (Lechatelierite). *Bulletin de la Societe Francaise de Mineralogie* 38: 182.

Lafuente, B., Downs, R. T., Yang, H., and Stone, N. 2015. 1. The Power of Databases: The RRUFF Project. In *Highlights in Mineralogical Crystallography*, edited by T. Armbruster, and R. M. Danisi, 1–30. Berlin: De Gruyter. https://doi.org/10.1515/9783110417104-003.

Levien, L., and Prewitt, C. T. 1981. High-Pressure Crystal Structure and Compressibility of Coesite. *American Mineralogist* 66: 324–333.

Liu, L. G. 1980. New High Pressure Phases of ZrO_2 and HfO_2. *Journal of Physics and Chemistry of Solids* 41: 331–34. https://doi.org/10.1016/0022-3697(80)90205-X.

MacDonald, A., Ubide, T., Mollo, S., Masotta, M., and Pontesilli, A. 2022. Trace Element Partitioning in Zoned Clinopyroxene as a Proxy for Undercooling: Experimental Constraints from Trachybasaltic Magmas. *Geochimica et Cosmochimica Acta* 336: 249–268. https://doi.org/10.1016/j.gca.2022.09.007.

Martell, J., Alwmark, C., Woracek, R., Alwmark, S., Hall, S., Ferrière, L., Daly, L., et al. 2024. Combined Neutron and X-Ray Tomography—A Versatile and Non-Destructive Tool in Planetary Geosciences. *Journal of Geophysical Research: Planets* 129: 1–15. https://doi.org/10.1029/2023JE008222.

Martin, A. J. 1969. Possible Impact Structure in Southern Cyrenaica, Libya. *Nature* 223: 940–41.

Moerhuis, N., Scoates, J. S., Weis, D., Scoates, R. F. J., and Tegner, C. 2025. Zircon Morphology and Geochemical Diversity during Closed-System Crystallization of the Skaergaard Intrusion. *Journal of Petrology* 66: egaf030. https://doi.org/10.1093/petrology/egaf030.

Murali, A. V., Linstrom, E. J., Zolensky, M. E., Underwood, J. R., and Giegengack, R. F. 1989. Evidence of Extraterrestrial Components in the Libyan Desert Glass. *EOS Transactions, American Geophysical Union* 70: 1178.

Murali, A. V., Zolensky, M. E., Underwood, J. R., and Giegengack, R. F. 1997. Chondritic Debris in Libyan Desert Glass. In *Proceedings of the Silica '96 Meeting on Libyan Desert Glass and Related Desert Events*, edited by V. De Michele, 133–142. Milan: Pyramids.

Orti, L., Di Martino, M., Morelli, M., Cigolini, C., Pannelli, E., and Buzzigoli, A. 2008. Non-impact Origin of the Crater-like Structures in the Gilf Kebir Area (Egypt): Implications for the Geology of Eastern Sahara. *Meteoritics & Planetary Science* 43: 1629–39. https://doi.org/10.1111/j.1945-5100.2008.tb00633.x.

Paillou, P., El-Barkooky, A., Barakat, A., Melezieux, J. M., Reynard, B., Dejax, J., and Heggy, E. 2004. Discovery of the Largest Impact Crater Field on Earth in the Gilf Kebir Region, Egypt. *Compte Rendus Géoscience de l'Académie de Sciences* 336: 1491–1500. https://doi.org/10.1016/j.crte.2004.09.010.

Paillou, P., Reynard, B., Melezieux, J. M., Dejax, J., Heggy, E., Rochette, P., Reimold, W. U., et al. 2006. An Extended Field of Crater-Shaped Structures in the Gilf Kebir Region, Egypt: Observations and Hypotheses about their Origin. *Journal of African Earth Sciences* 46: 281–299. https://doi.org/10.1016/j.jafrearsci.2006.05.006.

Palatinus, L., Brázda, P., Jelìnek, M., Hrdá, J., Steciuk, G., and Klementova, M. 2019. Specifics of the Data Processing of Precession Electron Diffraction Tomography Data and their Implementation in the Program PETS2.0. *Acta Crystallographica* 75: 512–522. https://doi.org/10.1107/S2052520619007534.

Peacor, D. R. 1973. High-Temperature Single-Crystal Study of the Cristobalite Inversion. *Zeitschrift für Kristallographie* 138: 274–298. https://doi.org/10.1524/zkri.1973.138.jg.274.

Pluth, J. J., Smith, J. V., and Faber, J. 1985. Crystal Structure of Low Cristobalite at 10, 293, and 473 K: Variation of Framework Geometry with Temperature. *Journal of Applied Physics* 57: 1045–49. https://doi.org/10.1063/1.334545.

Pratesi, G., Viti, C., Cipriani, C., and Mellini, M. 2002. Silicate-Silicate Liquid Immiscibility and Graphite Ribbons in Libyan Desert Glass. *Geochimica et Cosmochimica Acta* 66: 903–911. https://doi.org/10.1016/S0016-7037(01)00820-1.

Reimold, U., and Koeberl, C. 2014. Impact Structures in Africa: A Review. *Journal of African Earth Sciences* 93: 57–175. https://doi.org/10.1016/j.jafrearsci.2014.01.008.

Rocchia, R., Robin, E., Fröhlich, F., Ambosse, J., Barrat, J. A., Méon, H., Froget, L., and Diemer, E. 1997. The Impact Origin of Libyan Desert Glass. In *Proceedings of the Silica '96 Meeting on Libyan Desert Glass and Related Desert Events*, edited by V. De Michele, 143–49. Milan: Pyramids.

Sanità, E., Conconi, R., Lorenzon, S., Di Rosa, M., Capitani, G., and Mugnaioli, E. 2024. Application of an Improved TEM-EDS Protocol Based on Charge Balance for Accurate Chemical Analysis of Sub-Micrometric Phyllosilicates in Low-Grade Metamorphic Rocks. *Clays and Clay Minerals* 72: 1–11. https://doi.org/10.1017/cmn.2024.32.

Saul, J. M. 2018. Flickering Flames over the Libyan Desert? *International Geology Review* 61: 1–30. https://doi.org/10.1080/00206814.2018.1512057.

Schaaf, P., and Müller-Sohnius, D. 2002. Strontium and Neodymium Isotopic Study of Libyan Desert Glass: Inherited Pan-African Age Signatures and New Evidence for Target Material. *Meteoritics & Planetary Science* 37: 565–576. https://doi.org/10.1111/j.1945-5100.2002.tb00839.x.

Schneider, C. A., Rasband, W. S., and Eliceiri, K. W. 2012. NIH Image to ImageJ: 25 Years of Image Analysis. *Nature Methods* 9: 671–75. https://doi.org/10.1038/nmeth.2089.

Schneider, H., and Komarneni, S. 2006. *Mullite*. Weinheim: Vch Verlagsgesellschaft Mbh. 487. https://doi.org/10.1002/3527607358.

Sighinolfi, G., Lugli, F., Piccione, F., Michele, V., and Cipriani, A. 2020. Terrestrial Target and Melting Site of Libyan Desert Glass: New Evidence from Trace Elements and Sr Isotopes. *Meteoritics & Planetary Science* 55: 1865–83. https://doi.org/10.1111/maps.13550.

Spencer, L. J. 1939. Tektites and Silica-Glass. *Mineralogical Magazine and Journal of the Mineralogical Society* 25: 425–440.

Storzer, D., and Wagner, G. A. 1977. Fission-Track Dating of Meteorite Impacts. *Meteoritics* 12: 368–69.

Svetsov, V., Shuvalov, V., and Kosarev, I. 2020. Formation of Libyan Desert Glass: Numerical Simulations of Melting of Silica Due to Radiation from near-Surface Airbursts. *Meteoritics & Planetary Science* 55: 895–910. https://doi.org/10.1111/maps.13470.

Takagi, S., Ichiyanagi, K., Kyono, A., Kaway, N., Nozawam, S., Ozaki, N., Seto, Y., et al. 2022. Phase Transition and Melting in Zircon by Nanosecond Shock Loading. *Physics and Chemistry of Minerals* 49: 1–9. https://doi.org/10.1007/s00269-022-01184-8.

Telle, R., Greffrath, F., and Prieler, R. 2015. Direct Observation of the Liquid Miscibility Gap in the Zirconia-Silica System. *Journal of the European Ceramic Society* 35: 3995–4004. https://doi.org/10.1016/j.jeurceramsoc.2015.07.015.

Wang, N., Dai, S., Wang, X., Nechaev, V. P., French, D., Graham, I. T., Zhao, L., Song, X., and Song, X. 2022. New Insights into the Origin of Middle to Late Permian Volcaniclastics (Nb-Zr-REY-Ga-Rich Horizons) from Eastern Yunnan, SW China. *Lithos* 420-421: 106702. https://doi.org/10.1016/j.lithos.2022.106702.

Warr, L. N. 2021. IMA-CNMNC Approved Mineral Symbols. *Mineralogical Magazine* 85: 291–320. https://doi.org/10.1180/mgm.2021.43.

Weeks, R. A., Underwood, J. R., and Giegengack, R. 1984. Libyan Desert Glass: A Review. *Journal of Non-Crystalline Solids* 67: 593–619. https://doi.org/10.1016/0022-3093(84)90177-7.

Wei, P. H. 1935. Die Bindung im Quarz. *Zeitschrift für Kristallographie* 92: 355–362.

Wyckoff, R. 1926. Kriterien fur hexagonale Raumgruppen und die Kristallstruktur von beta Quarz. *Zeitschrift für Kristallographie* 63: 507–537. https://doi.org/10.1524/zkri.1926.63.1.507.

Zhao, J., Zhang, X., Xiao, L., Cavosie, A. J., Timms, N. E., Nemchin, A., Xiao, Z., et al. 2024. Nanoscale Constraints on the Nucleation and Evolution of Granular Zircon from Reidite in Impactites at the Chicxulub Impact Structure. *Earth and Planetary Science Letters* 626: 118507. https://doi.org/10.1016/j.epsl.2023.118507.

SUPPORTING INFORMATION

Additional supporting information may be found in the online version of this article.

Figure S1. Transmission electron microscopy-bright-field (TEM-BF) overview of the studied lamella.

Table S1. Energy-dispersive spectroscopy analysis performed on selected zircon crystals ($n = 111$).

Table S2. Energy-dispersive spectroscopy analysis of Libyan Desert Glass matrix (LDG) and interstice-filling glass (IF) ($n = 19$).